IEEE Access
Multidisciplinary | Rapid Review | Open Access Journal

Received April 26, 2020, accepted May 12, 2020, date of publication May 19, 2020, date of current version June 3, 2020.

Digital Object Identifier 10.1109/ACCESS.2020.2995652

An Improved Analytical Model of Permanent Magnet Eddy Current Magnetic Coupler Based on Electromagnetic-Thermal Coupling

XIAOWEI YANG, YONGGUANG LIU, AND LIANG WANG
School of Automation Science and Electrical Engineering, Beihang University, Beijing100191, China
Corresponding author: Xiaowei Yang (l_yangxiaowei@163.com)

This work was supported in part by the National Natural Science Foundation of China under Grant 11872006.

ABSTRACT There is a serious nonlinear between the sensitive parameters and the transmission capacity of the permanent magnet eddy current magnetic coupler (PMEC), and how to establish the accurate analytical model is very important to study its characteristics, optimize design and improve control accuracy. In order to solve the problem that the accuracy of analytical model deteriorates under the variable parameters of the PMEC, based on the electromagnetic-thermal theory, the electromagnetic-thermal nonlinearity of materials, such as the thermal effect of magnetic properties, the thermal effect of permeability, the thermal effect of conductivity, the magnetic saturation effect, the skin effect, the eddy current inductive reactance, have been deeply studied in this paper. On this basis, the multi-field coupling analytical model of the PMEC sensitive parameters and material electromagnetic thermal nonlinearity is established by using the magnetic equivalent circuit theory and lumped parameter thermal network method. Combined with numerical simulation and experiment, the research on electromagnetic characteristics, temperature characteristics and transmission characteristics of the PMEC are carried out. The comparative study shows that the proposed analytical model can accurately analyze the electromagnetic characteristics, temperature characteristics and transmission characteristics of the PMEC without any correction coefficient under different parameters. The accuracy of the analytical model with variable parameters is effectively solved, and the model theory of the PMEC is improved. The accurate analytical modeling method has laid theoretical foundation for the rapid optimization design and wide application of the PMEC.

INDEX TERMS The permanent magnet eddy current magnetic coupler, the accuracy of analytical model, the electromagnetic-thermal nonlinearity of materials, electromagnetic characteristics, temperature characteristics, transmission characteristics.

NOMENCLATURE

h_r	Thickness of the PM [mm]
h_c	Thickness of copper rotor [mm]
h_{ce}	Effective Thickness of copper rotor [mm]
h_F	Thickness of copper rotor back iron [mm]
h_b	Thickness of the PM back iron [mm]
g	Air gap [mm]
r_1	Inner diameter of the PM [mm]
r_2	Outer diameter of the PM [mm]
r_3	Inner diameter of copper rotor [mm]
r_4	Outer diameter of copper rotor [mm]
θ_0	Peripheral angle of the PM unit
N_1	Rotation speed of copper rotor[rpm]
N_2	Rotation speed of the PM rotor [rpm]
s	Slip between copper rotor and the PM rotor[%]
R_r	Reluctance of the PM[H^{-1}]
R_c	Reluctance of copper rotor [H^{-1}]
R_a	Reluctance of air gap [H^{-1}]
R_F	Reluctance of copper rotor back iron [H^{-1}]
R_b	Reluctance of the PM back iron [H^{-1}]
R_{a1}	Reluctance of the PM self-leakage [H^{-1}]
R_{a2}	Reluctance of the adjacent PM [H^{-1}]
φ_r	Flux source of the PM [Wb]
φ_e	Effective flux through copper rotor[Wb]
S_r	Surface area of the PM [m^2]

The associate editor coordinating the review of this manuscript and approving it for publication was Lei Zhao.

α	PM ratio
p	Pole pairs
μ_0	Vacuum permeability[H/m]
μ_r	Relative permeability of the PM
θ	Angle in circumferential direction [rad]
B_r	Remanence of the PM[T]
B_e	Static effective magnetic field intensity[T]
B_p	Induced magnetic field intensity[T]
B_{pe}	Dynamic coupling magnetic field intensity[T]
σ_c	Conductivity of copper rotor [MS/m]
σ_{pe}	Effective conductivity of copper rotor [Ms/m]
ω	Relative angular velocity [rad/s]
t_1	Temperature of the PM back iron [°C]
t_2	Temperature of the PM[°C]
t_3	Temperature of air gap [°C]
t_4	Temperature of copper rotor [°C]
t_5	Temperature of copper rotor back iron [°C]
t_6	Temperature of the PM mounted rotor [°C]
t_7	Ambient temperature [°C]
P_w	Heating power of copper rotor [w]

I. INTRODUCTION

The traditional connection has the disadvantage of small misalignment tolerance, which is the main reason for the failure of rotating machinery [1], [2]. Therefore, scholars have been exploring magnetic coupling drive technology, it has the advantages of large allowable misalignment, vibration isolation and noise reduction, no harmonic pollution, etc. [3] The permanent magnet eddy current magnetic coupler (PMEC) relates to the electromagnetic thermal multi-field coupling. How to establish accurate model is the basis of study the performance of the PMEC, optimal design and shafting. At present, the research methods mainly focus on numerical simulation and analytical method [4], [5].

The finite element method (FEM) is the representative of the numerical method. Li Z *et al.* studied the effect of slip on torque by using 3-D FEM, the validity of FEM is verified by experiments [6]–[8]. However, the FEM has a long calculation period, which is not conducive to rapid optimization, especially in the initial design stage, it is difficult to meet the design [9], [10]. The analytical method mainly includes Maxwell equations (ME) and magnetic equivalent circuit (MEC). Based on the ME, the control equations of each layer field domain were established under certain simplified conditions, and the expression of the torque was obtained by simplifying the method of variable separation. The torque expression was discretized, and combined with the boundary conditions of each layer field, the torque expression was solved [11]–[17]. However, the factors such as magnetic circuit saturation and magnetic leakage were difficult to be accurately reflected in the analytical model, which leaded to the low accuracy of the analytical model based on ME. The MEC compares the magnetic circuit with the electric circuit, and factors such as magnetic circuit saturation, nonlinearity of ferromagnetic materials, interaction between permanent magnetic field and reactive magnetic field, etc. can be considered. The magnetoresistance network model is constructed by using the magnetoresistance varying with time and space, and the network equation is established by the magnetic potential of the node, and the magnetic field distribution is obtained. The EMC can effectively balance the calculation time and accuracy, and it is suitable for the initial and optimal design of electromagnetic equipment [18]–[20]. Based on the MEC, Mohammadi s *et al.* ignored the electromagnetic-thermal nonlinearity of material, for example, only the resistance characteristics of the copper rotor were considered and the inductance characteristics were ignored, the thickness of the copper rotor, the working temperature, magnetic properties of the permanent magnet (PM) and the permeability of the back iron were set as fixed values. The transmission analytical model of the PMEC was established and compared with the FEM and experiment [21]–[24]. The results showed that the analytical model was not always accurate. Based on the parameter table in literature, the accuracy of the model was high in the range of low slip. If the parameter value was changed or the slip was increased, the model accuracy was reduced. For example, the air gap thickness increases from 4mm to 8.5mm, and the error increases by 1.4 times. The number of the PMs increased from 8 to 16, and the error increased from -2% to 7%. The analytical model can accurately analyze the transmission capacity of the PMEC under 5% slip, however, with the increase of slip, the accuracy of the analytical model was deteriorating. When the slip exceeded 15%, the model error was almost unacceptable. In order to solve this problem, a correction coefficient was introduced in document [25], which was a function of slip and had no clear physical meaning. Only under certain parameters, the accuracy of the modified model was high, but if the parameters were changed, such as the air gap thickness was changed, the model precision was reduced. In references [26], [27], inductance characteristics were introduced under constant temperature, and the model accuracy was greatly improved. However, in the industrial transmission system, the transmission condition and the ambient temperature of the PMEC changed greatly, it is impossible to keep the working temperature of the PMEC unchanged. The transmission conditions of the PMEC are various and the transmission power range is wide. If the electromagnetic thermal nonlinearity of the material is neglected, it is difficult to guarantee the accuracy of the transmission analytical model when the transmission power, the transmission condition or the ambient temperature change, which becomes the bottleneck of the fast optimization design of the PMEC.

In this paper, the mechanism research of the PMEC is carried out. Combined with electromagnetic thermal theory, the sensitive parameters are comprehensively revealed, the electromagnetic-thermal nonlinear characteristics of mater-ials is deeply studied. The analytical models of the electro-magnetic thermal characteristics, such as the thermal effect of magnetic properties, the thermal effect of permeability, the thermal effect of conductivity, the magnetic

saturation effect, the skin effect, the eddy current inductive reactance, are established. On this basis, combined with the MEC, lumped parameter thermal network theory (LPNT) and heat transfer theory, the analytical model of the PMEC including sensitive parameters and electromagnetic thermal character-istics of material is proposed. Through the comparative study of the unimproved analytical model, the FEM and experiment, without any correction coefficient, the improved analytical model can accurately analyze the electromagnetic characteristics, temperature characteristics and transmission capacity of the PMEC under different parameters. The influence of the sensitive parameters on the electromagnetic field, temperature field and transmission capacity of the PMEC are summarized, and the precise modeling method provides a new way for the fast optimization design of the PMEC.

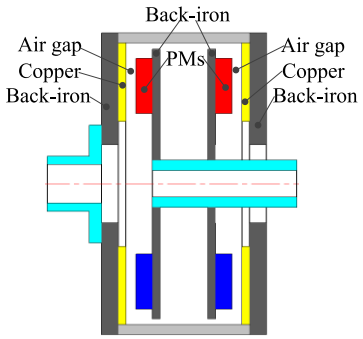

FIGURE 1. Schematic diagram of the PMEC.

II. STUDY ON THE MECHANISM OF THE PMEC

A. ELECTROMAGNETIC-THERMAL MULTI-FIELD COUPLING ANALYSIS OF THE PMEC

The structure of the PMEC is shown in Fig.1, including two permanent magnet (PM) rotors and two copper rotors, which are symmetrically distributed.

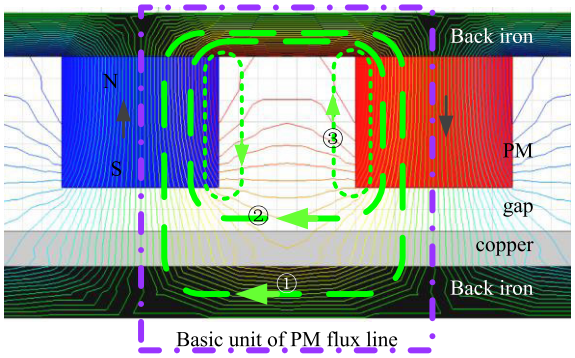

FIGURE 2. Distribution of magnetic field lines of the PM.

The FEM of the PM is shown in Fig. 2, and the distribution of magnetic field lines is summarized as follows.

① represents the magnetic circuit of the magnetic field line passing through the copper rotor back iron, ② represents the magnetic circuit of the magnetic field line not passing through the copper rotor back iron, ③ represents the magnetic circuit of the PM itself. Based on the analysis of the distribution of magnetic field lines, the MEC is adopted to establish the magnetic circuit diagram as shown in Fig. 3. the PM is equivalent to the current source, and the back iron, copper rotor, and air gap are equivalent to the resistance. In Fig. 3, the magnetic circuit represented by ①, ② and ③ is consistent with that in Fig. 2.

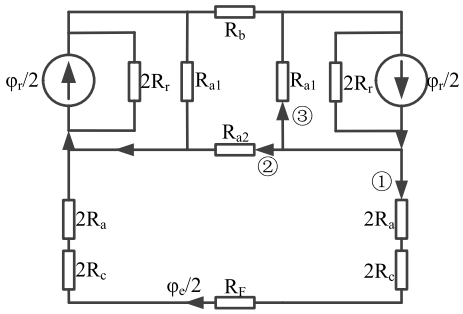

FIGURE 3. MEC analysis diagram.

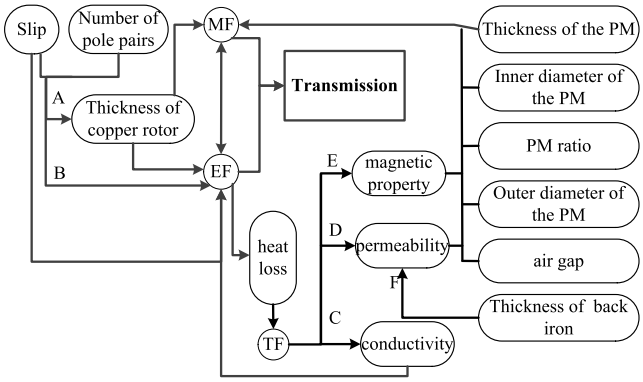

FIGURE 4. Relation diagram of the influence of sensitive parameters on transmission performance.

On the basis of magnetic circuit analysis, the relationship between sensitive parameters and transmission performance is summarized as shown in Fig. 4, MF is the magnetic field, EF is the eddy current field, TF is the temperature field, A is the skin effect, B is eddy current induced reactance, C is thermal effect of conductivity, D is the thermal effect of reluctance; E is the thermal effect of PM, F is saturation effect. Structural and electromagnetic parameters affect the strength of the magnetic field. slip and magnetic field affect the strength of eddy current field. The magnetic field and eddy current field determines the transmission performance of the PMEC. The heat loss affects the temperature field and the electromagnetic parameters of the material. The electromagnetic parameters of materials affect the eddy current heat loss. If the thickness of the back iron is too thin, the magnetic density will be too high, which will lead to the saturation effect and affect the permeability of the back iron. The slip and the pole pairs determine the alternating frequency of the eddy current. The alternating frequency determines the skin effect and the inductive reactance.

B. EFFECT OF EDDY CURRENT HEAT LOSS ON MAGNETIC PROPERTIES OF THE PM

The calculation expression of magnetic field strength at operating temperature is shown in Eq. 1.

$$B_{rt} = B_{r0}\left[1 + \alpha_B\left(t_2 - 20\right)\right] \tag{1}$$

in which, B_{rt} is the magnetic induction strength at t_2; B_{r0} is the magnetic induction strength at 20°C; α_B is the temperature coefficient of the PM.

C. EFFECT OF EDDY CURRENT HEAT LOSS ON CONDUCTIVITY OF COPPER

The conductivity of copper is the reciprocal of the resistivity, and the resistivity is approximately linear with the temperature. Eq. 2 is used to measure the effect of temperature on the resistivity.

$$\rho_t = \rho_0\left[1 + a_c\left(t_4 - 20\right)\right] \tag{2}$$

in which, ρ_t is the resistivity of copper at t_4, ρ_0 is the resistivity of copper at 20°C, α_c is the resistivity temperature coefficient of copper, the effect of temperature on conductivity is shown in Eq. 3.

$$\sigma_c = \frac{\sigma_0}{1 + a_c\left(t_4 - 20\right)} \tag{3}$$

in which, σ_c is the conductivity of copper at t_4, σ_0 is the conductivity of copper at 20°C.

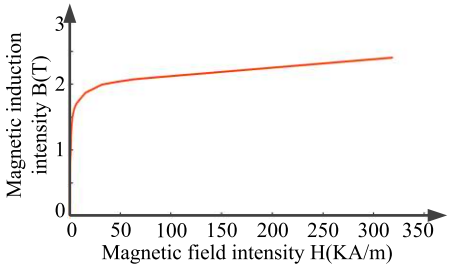

FIGURE 5. B-H curve of back iron [27].

D. INFLUENCE OF BACK IRON THICKNESS AND HEAT LOSS ON PERMEABILITY OF BACK IRON

The calculation of the magnetic flux density of the back iron is shown in Eqs. 4-5, B_b is the back flux density of permanent magnet, B_F is the back flux density of copper rotor. Fig. 5 is the B-H curve [27], and the relative permeability of back iron μ_b and μ_F are determined according to the B-H.

$$B_b = \frac{\varphi_r/2}{h_b\left(r_2 - r_1\right)} \tag{4}$$

$$B_F = \frac{\varphi_e/2}{h_F\left(r_2 - r_1\right)} \tag{5}$$

The relative permeability of back iron is also affected by the temperature, as shown in Eq. 6-7.

$$\mu_b = \mu_{b20} + \mu_{b20} \cdot \alpha_\mu\left(t_1 - 20\right) \tag{6}$$

$$\mu_F = \mu_{F20} + \mu_{F20} \cdot \alpha_\mu\left(t_5 - 20\right) \tag{7}$$

in which, μ_b is the relative permeability of the PM back iron at t_1, μ_F is the relative permeability of the copper back iron at t_5.

E. THE EFFECT OF SLIP AND POLE PAIRS ON EFFECTIVE THICKNESS OF COPPER ROTOR

With the increase of slip and the number of poles, the frequency of eddy current on the copper rotor increases, and produces skin effect. The calculation of skin depth is as follows [28].

$$\delta = \sqrt{\frac{2}{w_1\sigma_c\mu_0\mu_c}} \tag{8}$$

in which, w_1 is angular frequency, $w_1 = 2\pi f$, $f = 2psN_1/60$, $s = (N_1 - N_2)/N_1$.

$$\delta = \sqrt{\frac{15}{\pi psN_1\sigma_c\mu_0\mu_c}} \tag{9}$$

Due to skin effect, eddy current density of copper rotor decreases exponentially along z direction, as shown in Eq. 10.

$$J_Z = Je^{-z/\delta} \tag{10}$$

where, J_Z is the eddy current density at z from the copper rotor surface, and j is the eddy current density on the copper rotor surface.

Δ is defined as the effective depth of eddy current density,

$$\int_0^\delta Je^{-z/\delta}dz = \int_0^\Delta Jdz \tag{11}$$

Eq. 11 is solved, $\Delta = \delta(1\text{-}1/e)$.

The effective thickness h_{ce} of copper rotor is

$$h_{ce} = \min\left\{h_c, \Delta\right\} \tag{12}$$

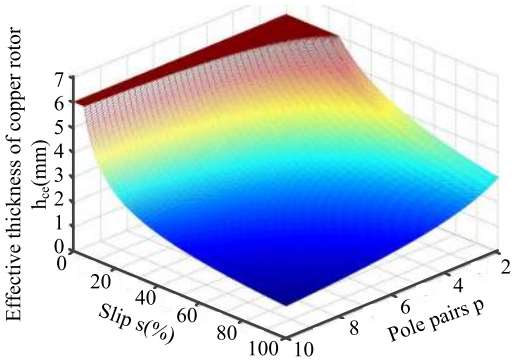

FIGURE 6. Relationship diagram of effective thickness of copper rotor.

Assuming the thickness of copper rotor is 6mm, the effect of slip and pole pairs on the effective thickness of copper rotor is shown in Fig. 6. When the slip and the pole pairs are small, the alternating frequency of eddy current is low and the skin effect is weak. The effective thickness of the copper rotor is the geometric thickness of the copper rotor. When the slip and the pole pairs are large, the frequency of eddy current is

high and the skin effect is obvious. The effective thickness of copper rotor is the skin depth.

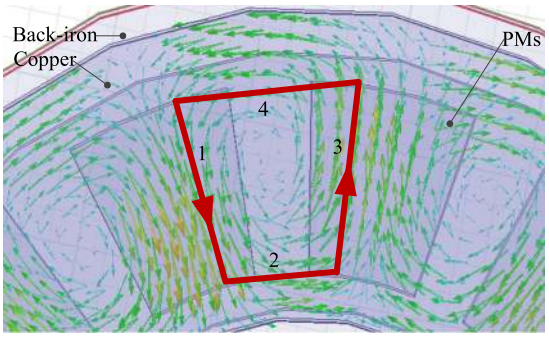

FIGURE 7. Eddy current distribution of copper rotor.

F. THE EFFECT OF SLIP AND POLE PAIRS ON EDDY CURRENT INDUCED REACTANCE

The Greenhouse method can quickly and accurately predict the rectangular spiral inductance, and the error range is less than 3% [26], [29], [30]. Based on FEM, the eddy current distribut-ion of copper rotor is shown in Fig. 7, according to the Greenhouse method in literatures [26], [29], The eddy current loop can be approximately regarded as a planar spiral inductor composed of four metal segments.

The total inductance L_M of copper rotor is [26], [29]

$$L_M = L_1 + L_2 + L_3 + L_4 - 2(M_{13} + M_{24}) \tag{13}$$

$$L_i = 2l_i\left(\ln\frac{2l_i}{h_{ce}+h_w} + 0.5 + \frac{h_{ce}+h_w}{3l_i}\right) \tag{14}$$

in which, L_i is the self-inductance of i segment conductor. li is the effective length of i segment conductor.

$$r_{AV} = \frac{r_1 + r_2}{2}$$

$$h_w = \frac{\alpha\theta_0 r_{AV}}{2}$$

Mutual inductance is calculated as follows [26], [29].

$$M_i = 2l_iQ_i \tag{15}$$

$$Q_i = \ln\left[\frac{l_i}{MD_i} + \left(1 + \frac{l_i^2}{MD_i^2}\right)^{1/2}\right] - \left(1 + \frac{MD_i^2}{l_i^2}\right)^{1/2} + \frac{MD_i}{l_i} \tag{16}$$

$$\ln MD_i = \ln d_i - \left\{\frac{1}{12\left(d_i/h_w\right)^2} + \frac{1}{60\left(d_i/h_w\right)^4} + \frac{1}{168\left(d_i/h_w\right)^6} + \ldots\right\} \tag{17}$$

in which, MD_{13} is the geometric mean distance of conductor segment 1 and segment 3, d_{13} is the center distance between conductor segment 1 and segment 3, MD_{24} is the geometric mean distance of conductor segment 2 and segment 4, d_{24} is the center distance between conductor segment 2 and segment 4.

The calculation for impedance is as follows.

$$Z = R_Z + jXL_M = |Z|\,e^{j\varphi_{R_Z}} \tag{18}$$

$$R_Z = \frac{l}{\sigma_c h_c h_w} \tag{19}$$

$$X = \frac{\pi spN_1}{15} \tag{20}$$

in which, Z is impedance, R_Z is resistance, σ_{pe} is defined as effective conductivity.

$$|Z| = \sqrt{\left(\frac{l}{\sigma_c h_c h_w}\right)^2 + \left(\frac{\pi psN_1L_M}{15}\right)^2} = \frac{l}{\sigma_{pe}h_c h_w} \tag{21}$$

$$\sigma_{pe} = \frac{\sigma_c}{\sqrt{1 + \left(\frac{\pi psN_1L_M h_w h_c \sigma_c}{15l}\right)^2}} \tag{22}$$

$$Cos\varphi_{R_Z} = R_Z/|Z| = \frac{\sigma_{pe}}{\sigma_c} = \frac{1}{\sqrt{1 + \left(\frac{\pi psN_1L_M h_w h_c \sigma_c}{15l}\right)^2}} \tag{23}$$

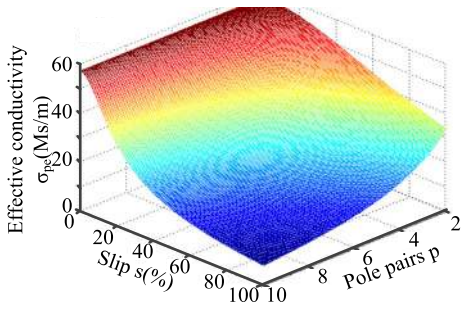

FIGURE 8. Effective conductivity of copper.

The effect of slip and pole pairs on the effective conductivity of copper is shown in Fig. 8. With the increase of slip and pole pairs, the alternating frequency of eddy current increases, the inductive reactance of eddy current increases, the impedance increases, and the effective conductivity of copper decreases.

III. STUDY ON THE MULTI-FIELD COUPLING MODDEL OF THE PMEC

A. ELECTROMAGNETIC MODEL OF THE PMEC

Based on section II, combined with MEC, the parameters in Fig. 3 are analyzed, and the electromagnetic model of the PMEC is established.

The internal resistance of the PM is as follows [26], [27].

$$R_r = \frac{h_r}{\frac{\alpha\theta_0}{2}\left(r_2^2 - r_1^2\right)\mu_0\mu_r} \tag{24}$$

The reluctance of the PM back iron is as follows.

$$R_b = \frac{1}{\int_{r_1}^{r_2} \frac{\mu_0 \mu_b h_b}{\alpha\theta_0 r} dr} \tag{25}$$

The reluctance of copper back iron is as follows [27].

$$R_F = \frac{1}{\int_{r_3}^{r_4} \frac{\mu_0 \mu_F h_F}{r\pi/p} dr} \tag{26}$$

The reluctance of air gap is as follows.

$$R_a = \frac{g}{\mu_0 \left(\alpha\theta_0 \frac{r_1+r_2}{2}\right)(r_2 - r_1)} \tag{27}$$

The reluctance of copper rotor is as follows.

$$R_c = \frac{h_c}{\mu_0 \left(\alpha\theta_0 \frac{r_1+r_2}{2}\right)(r_2 - r_1)} \tag{28}$$

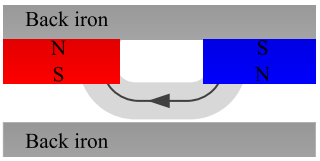

FIGURE 9. Analysis diagram of magnetic circuit ②.

In Fig. 2, ② and ③ are magnetic flux leakage, and the analysis of magnetic circuit ② is shown in Fig. 9. The reluctance of magnetic circuit ② is

$$R_{a2} = \frac{1}{\int_0^{r_{a2}} \frac{\mu_0 (r_2 - r_1)}{\pi r + \left(\frac{r_1+r_2}{2}\right)(1-\alpha)\theta_0} dr} \tag{29}$$

$$r_{a2} = \min\left\{\alpha\theta_0 \frac{r_1 + r_2}{4}, (g + h_c)\right\} \tag{30}$$

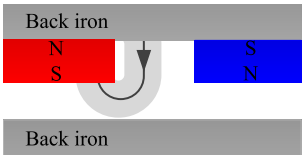

FIGURE 10. Analysis diagram of magnetic circuit ③.

The analysis of magnetic circuit ③ is shown in Fig. 10. ③ is the self-leakage magnetic circuit of the PM. The self-leakage of PM includes end leakage and side edge leakage, end leakage includes inner edge leakage and outer edge leakage [27]. The reluctance of side edge leakage is

$$R_{a11} = \frac{1}{\int_0^{r_{a11}} \frac{\mu_0 (r_2 - r_1)}{\pi r + h_r} dr} \tag{31}$$

$$r_{a11} = \min\left\{\alpha\theta_0 \frac{r_1 + r_2}{4}, (1 - \alpha)\theta_0 \frac{r_1 + r_2}{4}, (g + h_c)\right\} \tag{32}$$

The reluctance of inner edge leakage is

$$R_{a12} = \frac{1}{\int_0^{g+h_c} \frac{\mu_0 \alpha\theta_0 (r + r_1)}{\pi r + h_r} dr} \tag{33}$$

The reluctance of outer edge leakage is

$$R_{a13} = \frac{1}{\int_0^{g+h_c} \frac{\mu_0 \alpha\theta_0 (r_1 - r)}{\pi r + h_r} dr} \tag{34}$$

The self-leakage of PM can be expressed as [27]

$$\frac{2}{2/R_{a11} + 1/R_{a12} + 1/R_{a13}} = R_{a1} \tag{35}$$

Combined Eqs. 24-35, the effective flux φ_e is as follows

$$\varphi_e = \frac{4R_1 R_r}{R_1 (4R_{ac} + R_F) + 4R_r (4R_{ac} + R_F + R_1)} \varphi_r \tag{36}$$

in which, $R_{ac} = R_a + R_c$, $\varphi_e = B_{rt} S_r$, $R_1 = \frac{2R_{a1}(R_{a2}+R_b)}{2R_{a1}+R_{a2}+R_b}$.

$$B_e = \frac{\varphi_e}{S_r} \tag{37}$$

The static effective magnetic field strength is

$$B_e(\theta) = \begin{cases} \dfrac{4R_1 R_r B_{rt}}{R_1 (4R_{ac} + R_F) + 4R_r (4R_{ac} + R_F + R_1)} \\ \quad -\dfrac{\alpha\theta_0}{2} < \theta < \dfrac{\alpha\theta_0}{2} \\ 0 \\ \quad -\dfrac{\pi}{2p} < \theta < -\dfrac{\alpha\theta_0}{2}, \dfrac{\alpha\theta_0}{2} < \theta < \dfrac{\pi}{2p} \end{cases} \tag{38}$$

According to Faraday's law, copper rotor cuts magnetic field, and alternating eddy current is produced on copper rotor. Based on Ampere's law, induced eddy current produces induced magnetic field. The dynamic effective magnetic field is formed by the superposition of the induced magnetic field and the static effective magnetic field [26], [27].

$$B_{pe}(\theta) = B_e(\theta) + B_p(\theta) \tag{39}$$

Based on the Ampere's law, the calculation is [26], [27]

$$\oint_l Hdl = \iint_s Jds \tag{40}$$

Eq. 40 is substituted into Eq. 40.

$$\oint_l \frac{B_p(\theta)}{\mu_0} dl = \iint_s \sigma_{pe} r_{AV} \omega B_{pe}(\theta)\, ds \tag{41}$$

$$\frac{B_p(\theta)}{\mu_0} \cdot (2g + 2h_c + 2h_r) = \sigma_{pe}\omega r_{AV}^2 h_{ce} \int B_{pe}(\theta) d\theta \tag{42}$$

in which, $m = \frac{\mu_0 h_{ce} r_{AV}^2 \sigma_{pe}\omega}{2g+2h_c+2h_r}$.

According to Eq. 42,

$$B_p(\theta) = ke^{m\theta} + c \tag{43}$$

The general solution of $B_p(\theta)$ is derived as follows [26], [27].

$$B_p(\theta) = \begin{cases} k_1 e^{m\theta}, & \dfrac{-\pi}{2p} < \theta < \dfrac{-\alpha\pi}{2p} \\ k_2 e^{m\theta} - B_e, & \dfrac{-\alpha\pi}{2p} \le \theta \le \dfrac{\alpha\pi}{2p} \\ k_3 e^{m\theta}, & \dfrac{\alpha\pi}{2p} < \theta < \dfrac{\pi}{2p} \end{cases} \tag{44}$$

$B_p(\theta)$ meets Eq. 45-48 [26], [27].

$$B_p\left[\frac{-\alpha\pi}{2p}-0\right]=B_p\left[\frac{-\alpha\pi}{2p}+0\right] \tag{45}$$

$$B_p\left[\frac{\alpha\pi}{2p}-0\right]=B_p\left[\frac{\alpha\pi}{2p}+0\right] \tag{46}$$

$$B_p(\theta_1)=0 \tag{47}$$

$$\int_{\frac{-\pi}{2p}}^{\theta_1} Jh_{ce}r_{AV}d\theta=\int_{\theta_1}^{\frac{\pi}{2p}} Jh_{ce}r_{AV}d\theta \tag{48}$$

Based on the above conditions, $B_p(\theta)$ can be solved. In combination with Eq. 38 and Eq. 39, $B_{pe}(\theta)$ can be solved.

$$k_1=B_e\left[\frac{\cosh\left[(1-\alpha)\frac{m\pi}{2p}\right]}{\cosh\left[\frac{m\pi}{2p}\right]}-e^{\frac{\alpha\pi m}{2p}}\right] \tag{49}$$

$$k_2=B_e\frac{\cosh\left[(1-\alpha)\frac{m\pi}{2p}\right]}{\cosh\left[\frac{m\pi}{2p}\right]} \tag{50}$$

$$k_3=B_e\left[\frac{\cosh\left[(1-\alpha)\frac{m\pi}{2p}\right]}{\cosh\left[\frac{m\pi}{2p}\right]}-e^{\frac{-\alpha\pi m}{2p}}\right] \tag{51}$$

$$B_{pe}(\theta)=\begin{cases}k_1e^{m\theta} & \frac{-\pi}{2p}<\theta<\frac{-\alpha\pi}{2p}\\ k_2e^{m\theta} & \frac{-\alpha\pi}{2p}\le\theta\le\frac{\alpha\pi}{2p}\\ k_3e^{m\theta} & \frac{\alpha\pi}{2p}<\theta<\frac{\pi}{2p}\end{cases} \tag{52}$$

B. MODELING OF EDDY CURRENT THERMAL LOSS

The eddy current heat loss of the copper rotor is the heat source of the PMEC, and heat loss is very important to the temperature characteristic, the electromagnetic characteristic and the transmission characteristic. The eddy current heat loss is calculated as follows.

$$P_w=4pk_s\int_V\frac{|J|^2}{\sigma_c}dV \tag{53}$$

in which, k_s is the factor of eddy boundary effect [31].

$$k_s=1-\frac{\tanh(k_r)}{k_r\{1+\tanh(k)_r\tanh[p(r_4-r_3-r_2+r_1)/(2r_{AV})]\}} \tag{54}$$

in which, $k_r=p(r_2-r_1)/(2r_{AV})$.

The calculation expression of eddy current heat loss is

$$P_\omega=4pk_s\sigma_{pe}r_{AV}^2\omega^2Cos\varphi_{R_C}\int_V B_{pe}^2dV \tag{55}$$

C. STUDY ON TEMPERATURE CHARACTERISTICS OF THE PMEC

The heat generated by the copper rotor is dissipated through heat conduction, heat convection and heat radiation. Based on the LPTN, the eddy current loss of the copper rotor is regarded as the current source, the thermal resistance between components is regarded as the resistance, and the temperature is regarded as the potential. The equivalent heat grid diagram of the PMEC is established, as shown in Fig. 11.

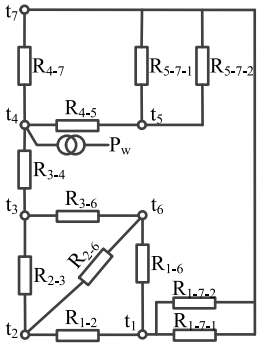

FIGURE 11. Equivalent thermal grid of the PMEC.

In Fig. 11, t_1 is the temperature of the PM back iron, t_2 is the temperature of the PM, t_3 is the temperature of air gap, t_4 is the temperature of copper rotor, t_5 is the temperature of the copper rotor back iron, t_6 is the temperature of the installed rotor, t_7 is the ambient temperature, P_W is the heating power of copper rotor, R_{1-7-1} is the convection thermal resistance between the PM back iron and air, R_{1-7-2} is the radiation thermal resistance between the PM back iron and air, R_{1-6} is the conduction thermal resistance between the PM back iron and the installed rotor, R_{1-2} is the conduction thermal resistance between the PM and the PM back iron, R_{2-6} is the conduction thermal resistance between the installed rotor and the PM, R_{2-3} is the convection thermal resistance between air gap and the PM, R_{3-6} is the convection thermal resistance between air gap and the installed rotor, R_{3-4} is the convection thermal resistance between copper rotor and air gap, R_{4-5} is the conduction thermal resistance between copper rotor and its back iron, R_{4-7} is the convection thermal resistance between copper rotor and air, R_{5-7-1} is the convection thermal resistance between copper rotor back iron and air, R_{5-7-2} is the radiation thermal resistance between copper rotor back iron and air. Based on the circuit research method and the heat transfer theory, the research of the Fig. 11 is carried out.

The conduction thermal resistance R_{1-6}, R_{1-2}, R_{2-6} and R_{4-5} are calculated as follows [16].

$$R=L_R/\lambda A \tag{56}$$

in which, λ is the thermal conductivity of the material, L_R is the length of heat transfer path, A is the heat flow area.

The convection heat resistance R_{1-7-1}, R_{4-7}, R_{5-7-1}, R_{3-6}, R_{2-3} and R_{3-4} are calculated as follows [32].

$$R = {}^{1}/_{h_t A} \tag{57}$$

In which, h_t is the convective heat transfer coefficient. The h_t calculation in R_{1-7-1}, R_{4-7} and R_{5-7-1} is shown in Eq. 58 [33], and the rest is shown in Eq. 59 [34].

$$h_t = 9.73 + 14v_t^{0.62} \tag{58}$$

$$h_t = {}^{N_u \lambda_{air}}/_{g} \tag{59}$$

in which, v_t is the velocity of air passing through the surface, λ_{air} is the thermal conductivity of air, and the calculation is shown in Eq. 60 [34], N_u is the Nusselt number, and the calculation is shown in Eq. 61 [34].

$$\lambda_{air} = 2.72 \times 10^{-4} \left(\frac{t_g + t_f}{2} \right)^{0.8} \tag{60}$$

where, t_g is the temperature of the gas, t_f is the temperature of the solid surface in contact with the gas.

$$N_u = \begin{cases} 2, & t_a \le 1700 \\ 0.128 t_a^{0.367}, & 1700 \le t_a \le 10^4 \\ 0.409 t_a^{0.241}, & 10^4 \le t_a \le 10^7 \end{cases} \tag{61}$$

t_a is the Taylor number, which is calculated as follows.

$$t_a = \left(\frac{v_r g}{\gamma_t} \right)^2 \frac{g}{r_4} \tag{62}$$

in which, v_r is the relative sliding speed, γ_t is the air kinematic viscosity, as shown in Eqs. 63-65 [34].

$$\mu_g = \mu_{15} \left(\frac{t_g}{288.15} \right)^{1.5} \frac{288.15 + t_B}{t_g + t_B} \tag{63}$$

$$\rho_g = 1.293 \times \frac{273.15}{t_g} \tag{64}$$

$$\gamma_t = \frac{\mu_g}{\rho_g} \tag{65}$$

in which, μ_{15} dynamic viscosity at 288.15k. t_B is a constant related to the type of gas.

R_{1-7-2} and R_{5-7-2} are radiation thermal resistances, which are calculated as follows [35].

$$R = \frac{1}{\varepsilon_t \delta_t A F_{12}} \tag{66}$$

ε_t is the radiation rate. F_{12} is the shape coefficient. δ_t is the blackbody radiation constant, $5.67 \times 10^{-8} \mathrm{W/(m^2 \cdot k)}$.

Combined with the theory of heat transfer and the LNPT, the heat transfer equations are established in the appendix.

D. ELECTROMAGNETIC THERMAL MULTIFIELD COUPLING MODEL OF THE PMEC

There is speed difference in the transmission process of the PMEC, and the energy loss is lost in the form of eddy current heat loss [22].

$$P_w = T\omega \tag{67}$$

T is the transmission capacity of the PMEC, combined with Eq. 53, it is calculated as follows.

$$T = 4p \frac{k_s}{\omega} \int_V \frac{|J|^2}{\sigma_c} dV = \frac{4pk_s \sigma_{pe}^2 v^2}{\sigma_c \omega} \int_V B_{pe}^2(\theta) dV \tag{68}$$

$$\begin{aligned} T = {} & \frac{2pk_s r_{AV}^3 (r_2 - r_1) h_{ce} \sigma_{pe} \omega Cos\varphi_{R_Z}}{m} \\ & \cdot \left[k_1^2 e^{\frac{-\alpha m\pi}{p}} - k_1^2 e^{\frac{-m\pi}{p}} + k_2^2 e^{\frac{\alpha m\pi}{p}} - k_2^2 e^{\frac{-\alpha m\pi}{p}} \right. \\ & \left. + k_3^2 e^{\frac{m\pi}{p}} - k_3^2 e^{\frac{\alpha m\pi}{p}} \right] \end{aligned} \tag{69}$$

The analytical model not only contains the sensitive parameters, but also contains the electromagnetic-thermal nonlinearity of materials, which guarantees the accuracy of the established transmission analytical model from the perspective of mechanism. The solution process is shown in Fig. 12. The electromagnetic, temperature and transmission characteristics of the PMEC are studied.

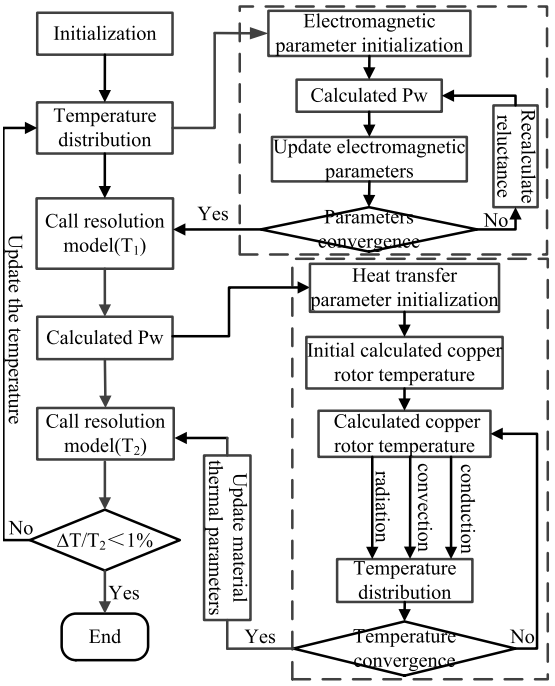

FIGURE 12. Flow chart of iterative analysis of analytical model.

IV. NUMERICAL SIMULATION STUDY ON MULTI-FIELD COUPLING OF THE PMEC

The structural parameters are shown in Table 1. Combined with the electromagnetic-thermal FEM, the comparative study of electromagnetic characteristics, temperature characteristics and transmission characteristics is carried out. The flow chart of multi-field coupling FEM is shown in Fig. 13, and the steps are as follows.

1) Combined with the structural parameters of the PMEC, the FEM model of the PMEC is established, as shown in Fig. 14.

TABLE 1. Parameters of the PMEC.

Symbol	Quantity	value
r_1	Inner diameter of the PM [mm]	107.5
r_2	Outer diameter of the PM [mm]	167.5
r_3	Inner diameter of copper rotor [mm]	95
r_4	Outer diameter of copper rotor [mm]	185
h_r	Thickness of the PM[mm]	20
h_c	Thickness of copper rotor [mm]	6
h_b	Thickness of the PM back iron [mm]	16
h_F	Thickness of copper rotor back iron [mm]	20
p	pole pairs	6
α	PM ratio	0.67

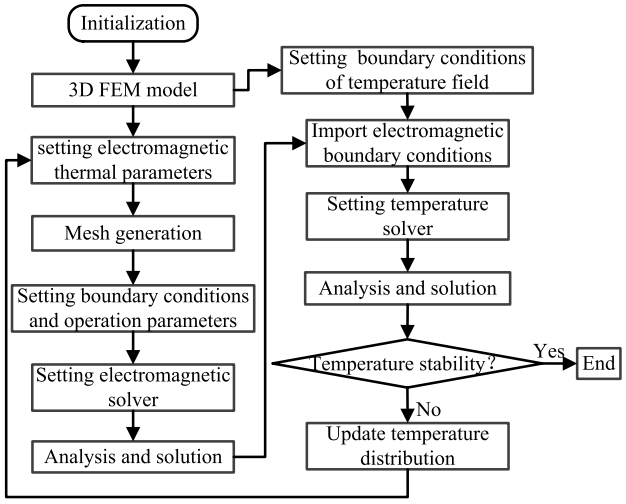

FIGURE 13. Flow chart of electromagnetic thermal multi field coupling.

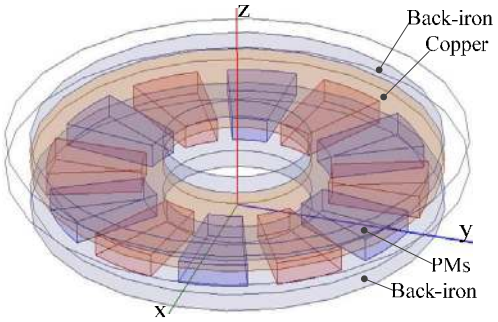

FIGURE 14. Three dimensional finite element model of the PMEC.

2) Determination of electromagnetic thermal parameters, including material electromagnetic parameters, electro-magnetic thermal effect coefficient and heat transfer coefficient.
3) The electromagnetic numerical simulation is studied, the FEM model is imported into the Maxwell 3D design module on the ANSYS Workbench platform, and the model is processed. Electromagnetic calculation model is selected, electromagnetic parameters and element types of materials are set, grids are divided, electro-magnetic boundary conditions and operation conditions are imposed, solvers are set, and transient electro-magnetic analysis is carried out.

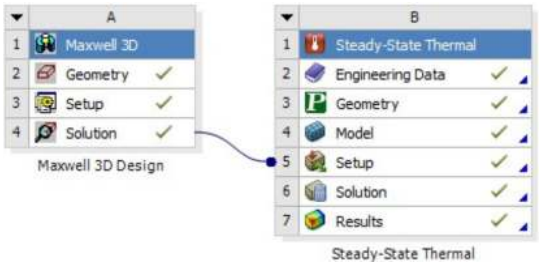

FIGURE 15. Electromagnetic thermal multi field coupling simulation diagram of the PMEC.

4) The electromagnetic numerical simulation results are imported into the steady-state Thermal module, as shown in Fig. 15. The eddy current heat loss is the temperature field heat source. The heat transfer coefficient of the material is set, the thermal boundary conditions are applied, and the solver is set to conduct the temperature field analysis. For example, when the air gap thickness is 4mm and slip is 12%, the temperature distribution of the PMEC is shown in Fig. 16.

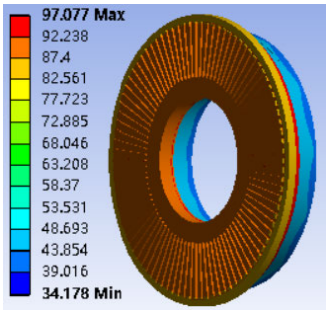

FIGURE 16. Temperature distribution of the PMEC (g = 4mm).

5) Compared the setting data of working temperature with simulation data. If Eq. 70 is satisfied, the iteration is stopped and electromagnetic distribution, electromagne-tic torque and temperature distribution are output. Otherwise, the temperature distribution according to Eq. 71 is updated, and the electromagnetic parameters of the material are updated based on the new temperature distribution. Returning to 3, the research of electromag-netic thermal simulation is carried out.

$$\left|\frac{t^{(k)} - t^{(k-1)}}{t^{(k)}}\right| \leq 0.01 \tag{70}$$

$$t^{(k+1)} = \left[t^{(k)}\right]^{0.5}\left[t^{(k-1)}\right]^{0.5} \tag{71}$$

The FEM is compared with the improved analytical model and the unimproved analytical model to verify the accuracy of the improved analytical model under different sensitive parameters.

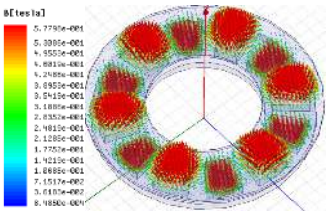

FIGURE 17. Distribution diagram of static effective magnetic field.

A. STUDY ON THE EFFECT OF AIR GAP THICKNESS AND SLIP ON ELECTROMAGNETIC CHARACTERISTICS

When the air gap thickness is 4mm, the static effective magnetic field distribution is shown in Fig. 17. The static effective magnetic field is generated by the PM. Most of the magnetic field lines start from the N-pole, pass through the air gap and the copper rotor, enter the back iron of the copper rotor, and then pass through the copper rotor and the air gap again to the S-pole of the adjacent PM.

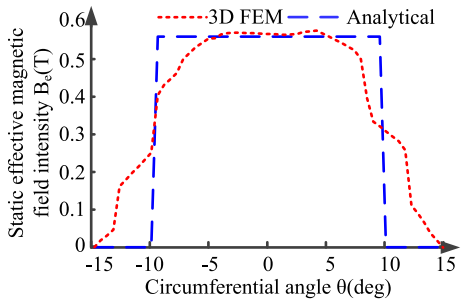

FIGURE 18. Distribution diagram of effective magnetic field (g = 4mm).

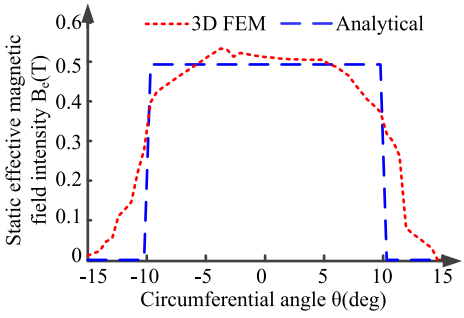

FIGURE 19. Distribution diagram of effective magnetic field (g = 6mm).

The distribution curve of static effective magnetic field is shown in Fig. 18 and Fig. 19. In the range of $-10°$ $\sim 10°$, the magnetic field is strong and evenly distributed, while in other intervals, the magnetic field is almost 0. The magnetic field is mainly distributed in the region corresponding to the PM. The analytical data are basically consistent with the FEM data, with an average error of 3.9%. This is because the increase in air gap thickness leads to the increase in air gap reluctance, which leads to the increase in magnetic leakage, so the effective magnetic field strength decreases.

When the air gap is 4mm, the distribution of dynamic effective magnetic field under 2% and 4% slip is shown

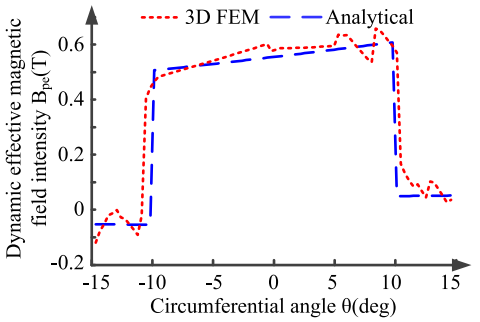

FIGURE 20. Distribution diagram of effective magnetic field (s = 2%).

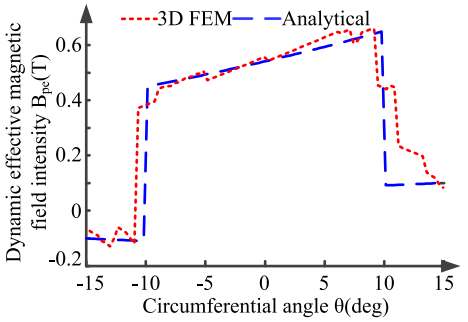

FIGURE 21. Distribution diagram of effective magnetic field (s = 4%).

in Fig. 20 and Fig. 21. Compared with the static effective magnetic field, the magnetic field intensity is negative in the range of $-15° \sim -10°$, positive in the range of $10° \sim 15°$, and gradually enhanced in the range of $-10° \sim 10°$. With the increase of slip, the influence of induced magnetic field on the magnetic field of the PMEC is enhanced.

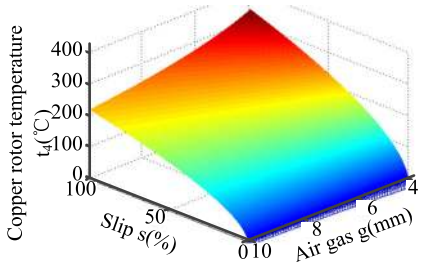

FIGURE 22. Influence of air gap and slip on temperature of copper rotor.

B. STUDY ON THE EFFECT OF AIR GAP THICKNESS AND SLIP ON TEMPERATURE CHARACTERISTICS

The influence of air gap thickness and slip on the temperature of copper rotor is shown in Fig. 22. The air gap is negatively related to the temperature rise of copper rotor. When the air gap thickness is 4mm, the temperature of copper rotor under different slip is as shown in Fig. 23. Within the range of 2%∼4% slip, the temperature of copper rotor shall not exceed 45°C. When the slip is 12%, the temperature of copper rotor reaches 97 °C. The FEM data is consistent with the analytical data, and the error range is no more than 2.9%.

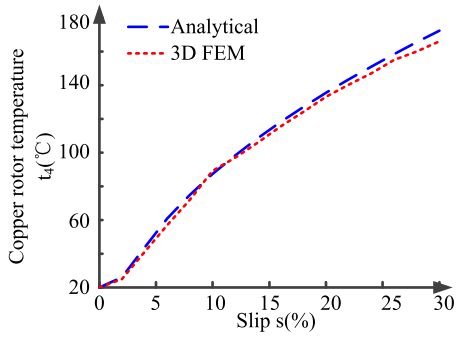

FIGURE 23. Temperature curve of copper rotor.

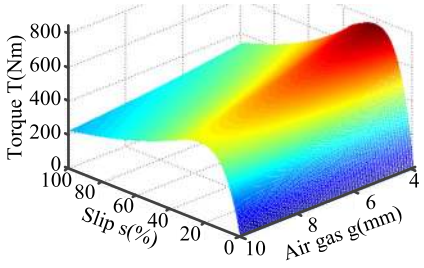

FIGURE 24. The influence of air gap thickness and slip on transmission capacity.

C. STUDY ON THE EFFECT OF AIR GAP THICKNESS AND SLIP ON TRANSMISSION CHARACTERISTICS

Based on the proposed transmission analytical model, the influence of slip and air gap on the transmission capacity of the PMEC is studied, as shown in Fig. 24. With the increase of air gap, the transmission capacity of the PMEC decreases. With the increase of slip, the transmission capability of the PMEC is enhanced, but when the slip exceeds a certain value, the transmission capability is decreased.

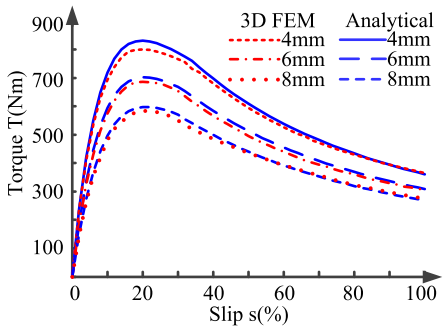

FIGURE 25. The influence of slip on the transmission capacity.

The thickness of air gap is 4mm, 6mm and 8mm, the influence rule of slip on the transmission capacity of the PMEC is shown in Fig. 25. In the range of 100% slip, the comparative study is as follows. Within 0∼20% slip, slip is positively correlated with the transmission capacity, slip is negatively correlated with the transmission capacity in 20%∼100% slip. Under different air gap thickness and slip, the variation law of FEM data is consistent with that of analytical data, and the position of peak torque inflection point is the same. The error range is no more than 3.9%.

When the slip is less than 20%, the eddy current intensity increases, which makes the driving force increase, and then the transmission capacity of the PMEC increases. When the slip is higher than 20%, the slip will continue to increase, and the induced magnetic field will weaken the effective magnetic field, thus reducing the effective magnetic field strength, and the driving force of magnetic coupling. So the transmission capacity of the PMEC is reduced.

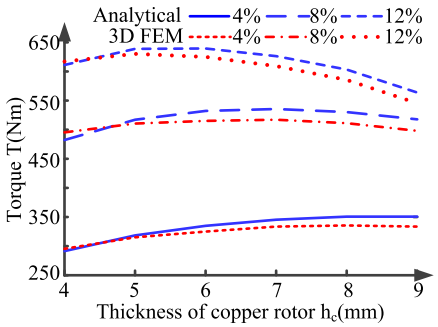

FIGURE 26. The influence of copper rotor thickness on transmission capacity(g = 6mm).

D. RESEARCH ON THE INFLUENCE OF COPPER ROTOR THICKNESS ON TRANSMISSION CAPACITY

The thickness of copper rotor is changed, and the FEM data is compared with the analytical data, as shown in Fig. 26. The variation of FEM data is consistent with that of analysis data. When the thickness of copper rotor is less than 5mm, the thickness of copper rotor is positively related to the transmission capacity, when the thickness of copper rotor is more than 6mm, the thickness of copper rotor is negatively related to the transmission capacity. With the increase of the thickness, the increase of the magnetoresistance will increase the flux leakage of the PM and reduce the effective magnetic field intensity. However, the increase of the copper rotor thickness is conducive to the enhancement of the eddy current field. The optimum thickness of the copper rotor is 6mm. The error between FEM data and analysis data is less than 4.1% under different slip and thickness of copper rotor.

E. STUDY ON THE INFLUENCE OF PM RATIO ON TRANSMISSION CAPACITY

The thickness of air gap is 6 mm, and the circumferential angles of the PM are 16°, 18°, 20°, 22°, 24°, 26°, 28°, respectively. The analytical data and FEM data are compared, as shown in Fig. 27. The PM ratio is positively related to the transmission capacity. The PM ratio is larger, the volume of the PM is larger, and the total magnetic flux is greater, so the transmission capacity of the PMEC is enhanced. When the PM ratio is more than 0.85, the distance between the PMs is very small, which makes the magnetic flux leakage increase

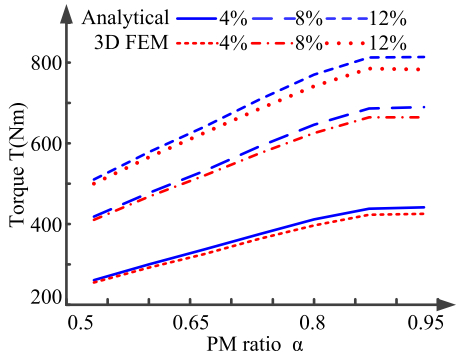

FIGURE 27. The influence of PM ratio on transmission capacity(g = 6mm).

rapidly and the utilization rate of magnetic energy decrease. The transmission capacity of the PMEC is almost unchanged. Under different slip and PM ratio, the variation law of the analytical data of transmission capacity is consistent with that of the FEM data, and the error range is no more than 3.6%.

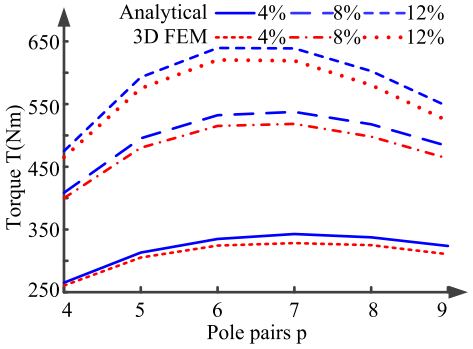

FIGURE 28. The influence of pole pairs on transmission capacity (g = 6mm).

F. STUDY ON THE INFLUENCE OF POLE PAIRS ON TRANSMISSION CAPACITY

When the air gap thickness is 6mm, only pole pairs is changed, and the total volume of the PM remains unchanged. The analytical data and FEM data are compared in depth, as shown in Fig. 28. When the pole pairs is less than 6, the pole pairs is reduced and the boundary effect of eddy current is enhanced, so the transmission capacity of the PMEC is decreased. When the pole pairs is greater than 7, increasing the pole pairs will reduce the distance between the PMs, the magnetic flux leakage increases and the effective magnetic field intensity reduces, so the transmission capacity of the PMEC will decrease. The optimum number of poles is 6. Under different slip, the error range of analysis data and FEM data is less than 3.9%, which further verifies the accuracy of the proposed analytical model.

G. RESEARCH ON THE INFLUENCE OF THE PM THICKNESS ON TRANSMISSION CAPACITY

The thickness of the PM is changed, and the analysis data of transmission capacity is compared with the FEM data, as shown in Fig. 29. The PM thickness has a positive

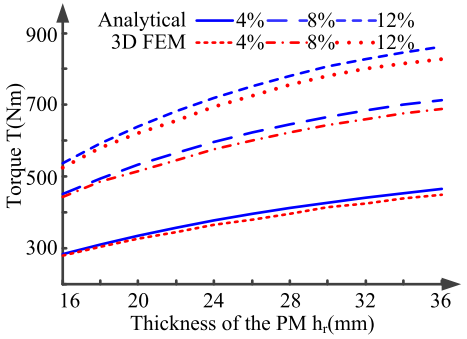

FIGURE 29. The influence of the PM thickness on transmission capacity (g = 6mm).

correlation with the transmission capacity of the PMEC. With the increase of the PM thickness, the effective magnetic flux increases. Under the same slip, the eddy current field in the copper rotor is strengthened, the driving force of the magnetic coupling is enhanced, and the transmission capacity of the PMEC is enhanced. The analytical data of transmission capacity is slightly larger than the FEM data under different thickness of the PM, and the error range is less than 3.5%.

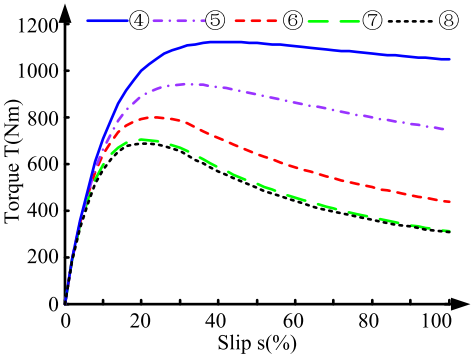

FIGURE 30. The comparison diagram of transmission model.

H. THE COMPARATIVE STUDY OF MODELS

The analytical model of the PMEC transmission ignores the electromagnetic thermal nonlinear characteristics of materials, such as the thermal effect of magnetic properties, the thermal effect of permeability, the thermal effect of conductivity, the magnetic saturation effect, the skin effect, the eddy current inductive reactance, and the accuracy of the transmission model is not always accurate. In view of this problem, the comparative study is conducted on the influence of the electromagnetic thermal nonlinear characteristics of materials on the model accuracy, as shown in Fig. 30 and Fig. 31. On the basis of Table 1, ignoring the electromagnetic thermal nonlinear characteristics of materials, B_r, σ_c, μ_b and μ_F are regarded as constants, and the analytical model of transmission is established. The relationship between slip and transmission capacity is shown in curve ④. Based on the analytical model proposed in this paper, the relationship between slip and transmission capacity is shown in curve ⑦. Curve ⑧ represents the relationship curve between slip and

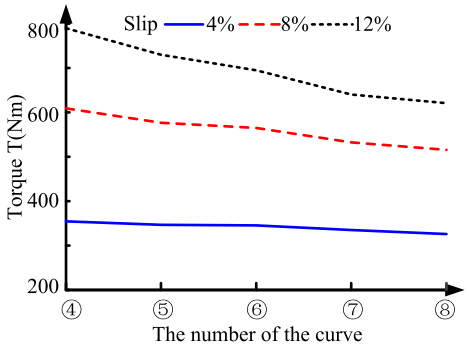

FIGURE 31. The comparison diagram of transmission model data under certain slip.

transmission capacity based on the FEM of electromagnetic thermal multi-field coupling. Comparative study shows that, within 100% slip, curve ⑦ is basically consistent with curve ⑧. Compare curve ④ with curve ⑧, the error range is not more than 5.5% within 5% slip, and when the slip is 8%, the error increases to 16%.

The reasons are as follows. When the slip is small, combined with the research of section III.B and section IV.B, the heating of the PMEC is very small, so the working temperature of the PMEC is very low. Combined with the analysis of sections II.B, II.C and II.D, the magnetic properties, permeability and conductivity have little influence. The results of section II.E and section II.F show that when the slip is small, the alternating frequency of eddy current is low, and the skin effect and inductive reactance are weak. Therefore, neglecting the nonlinear characteristics of the material has little effect on the accuracy of the analytical model. When the slip is large, combined with the research of section III.B and section IV.B, the heating of the PMEC is large, the working temperature is high, and the influence of magnetic properties, permeability and conductivity is large. Moreover, the large slip makes the alternating frequency of eddy current high, and the skin effect and the inductive reactance characteristics are strong. Therefore, the accuracy of the analytical model deteriorates with the increase of slip.

In order to investigate the influence of the thermal effect of the material, skin effect and inductive reactance of eddy current on the accuracy of the model, Curve ⑤ is the change curve of transmission capacity only considering thermal effect, curve ⑥ is the change curve of transmission capacity only considering inductive reactance and skin effect. Compared with curve ⑧, the results show that the nonlinear characteristics of material have a great influence on the accuracy of analytical model, especially the skin effect and inductive reactance of eddy current.

V. EXPERIMENTAL STUDY ON THE PMEC

In order to verify the proposed analytical model, transmission test platform of the PMEC is built, as shown in Fig. 32. The electromagnetic characteristics, temperature characteristics and transmission characteristics of the PMEC are studied. Considering the material properties and the safety of the

FIGURE 32. Physical diagram of the experimental platform.

experimental equipment, the temperature of the copper rotor shall not exceed 200 °C during the experiment [36].

A. RESEARCH ON ELECTROMAGNETIC CHARACTERISTICS

Under the static state of copper rotor and the PM copper, the measurement and control system controls the rotation of the output shaft of the actuator to drive the axial movement of the PM rotor. The tilt sensor measures the rotation angle of the output shaft, then the air gap thickness between the conductor rotor and the permanent magnet rotor is calculated to realize the semi closed loop control of the air gap thickness. Tesla meter is used to measure the effective magnetic field strength.

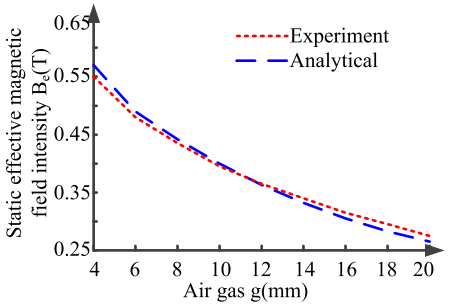

FIGURE 33. Relation curve between air gap and effective magnetic field strength.

The relationship between the air gap thickness and the effective magnetic field strength is shown in Fig. 33. The air gap thickness is negatively correlated with the effective magnetic field strength, and the error range between the experimental data and the analytical data is less than 3.3%, which verifies the validity of the analytical model.

B. RESEARCH ON TEMPERATURE CHARACTERISTICS

The copper rotor back iron and copper rotor are good heat conductors, in addition, the copper rotor back iron is in close contact with the copper rotor, and the contact surface is large. Therefore, the temperature difference between the copper rotor back iron and the copper rotor is very small. The temperature of copper rotor back iron can well reflect the temperature of copper rotor. In the experiment, infrared non-contact temperature sensor is used to measure the temperature of copper rotor back iron.

The measurement and control system controls the output shaft of the actuator to rotate so that the air gap thickness is 4mm. The measurement and control system controls the

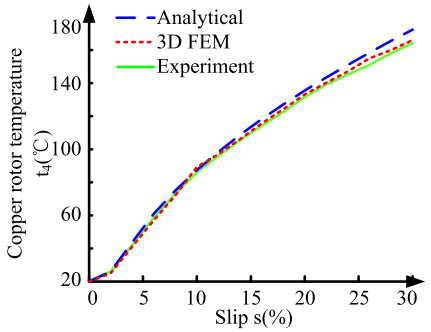

FIGURE 34. Temperature curve of copper rotor (g = 4mm).

output speed of the motor, and the torque sensor has the function of measuring the speed and torque. The comparison curve of experimental data, analytical data and FEM data is shown in Fig. 34. The variation law of experimental data, analytical data and FEM data is consistent, and the error range is no more than 3.8%. The air gap thickness is changed to 24mm, and the temperature curve is shown in Fig. 35. With the increase of air gap thickness, the working temperature of copper rotor decreases, and the error range of experimental data, analytical data and FEM data is less than 4.2%. The validity of the proposed analytical model is verified in the analysis of temperature field.

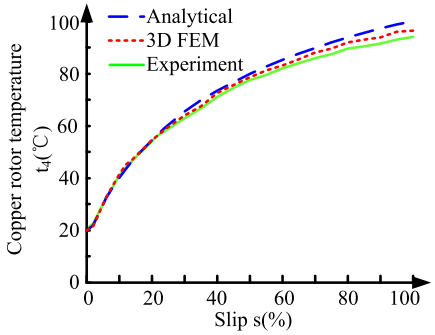

FIGURE 35. Temperature curve of copper rotor (g = 24mm).

C. RESEARCH ON TRANSMISSION CHARACTERISTICS

The measurement and control system controls the output speed of the motor, the torque sensor measures the speed and torque of the shafting, the actuator controls the air gap thickness to be 4mm, 6mm and 24mm respectively. According to the research of temperature field, when the air gap thickness is 4mm and 6mm, and the slip is 30%, the temperature of copper rotor is about 180 °C. Therefore, when the air gap thickness is 4mm and 6mm, the slip range of experimental test is 30%. When the air gap thickness is 4mm, the variation law of transmission characteristics is shown in Fig. 36. The analytical data presented in this paper, FEM data and experimental data are basically the same, and the error range is not more than 3.2%. The analytical data without electro-magnetic thermal nonlinearity of materials, FEM data and experimental data are compared, as the slip increases, the error increases, when the slip is 5%, the error is about 6%, when the slip

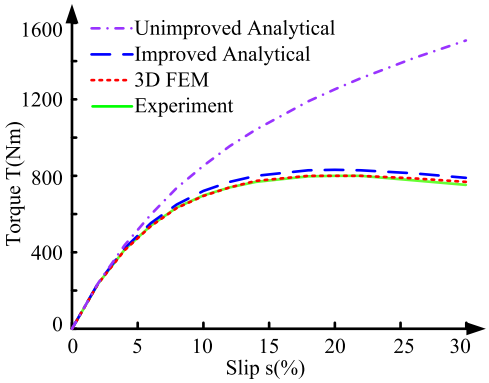

FIGURE 36. Transmission characteristic curve of the PMEC (g = 4mm).

is 14%, the error increases to 31%, when the slip is 30% and the error is more than 100%.

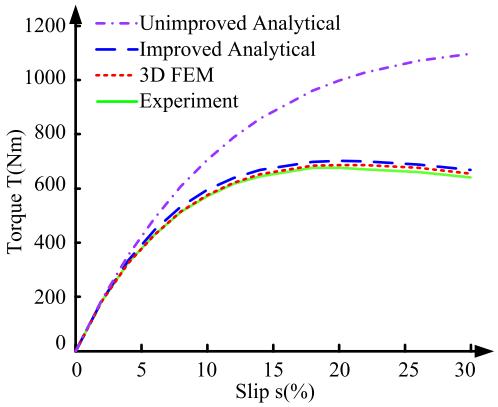

FIGURE 37. Transmission characteristic curve of the PMEC (g = 6mm).

The air gap thickness is 6mm, the variation rule of the transmission characteristics is shown in Fig. 37. The improved analytical data, FEM data and experimental data are in good agreement, the error shall not exceed 3.5%. However, the error of analytical data without the electromagnetic thermal nonlinearity of materials is small when the slip is less than 5%. With the increase of slip, the error increases continuously. When the slip is 14%, the error increases to 28%. When the slip is 30%, the error is 70%.

When the air gap thickness is 24mm, the transmission characteristics are shown in Fig. 38. The improved analytical data, FEM data and experimental data are compared. The error range shall not exceed 2.9%, and the error does not increase with the increase of slip. The error of the unimproved analytical data increases with the increase of the slip. When the slip is 5%, the error is 8%. When the slip is 14%, the error increases to 29.6%. When the slip is 30%, the error is 110%, and when the slip is 100%, the unimproved analytical data is about 6 times of the experimental data.

Through the comparative study of experiment, FEM, improved analytical model and unimproved analytical model, it is proved that the electromagnetic thermal nonlinearity

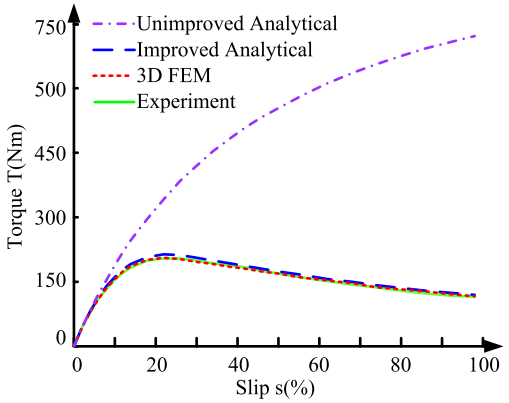

FIGURE 38. Transmission characteristic curve of the PMEC (g = 24mm).

of materials are important to the accuracy of the analytical model, and the accuracy of the analytical model proposed in this paper is verified.

VI. CONCLUSION

In order to solve the accuracy problem of the analytical model of the PMEC, this paper starts from the transmission mechanism of the PMEC, reveals the electromagnetic thermal nonlinear characteristics of materials, and establishes the analytical model of the electromagnetic-thermal multi-field coupling. Compared with unimproved analytical model, the FEM and the experiment, the improved analytical model can accurately analyze the electromagnetic characteristics, temperature characteristics and transmission characteristics of the PMEC. The summary is as follows.

1) The electromagnetic thermal nonlinear characteristics of materials is revealed. Eddy current heat loss, PM heat effect, conductivity heat effect, permeability heat effect, magnetic saturation effect, skin effect and eddy current inductive reactance characteristics are studied in depth. The general law of the sensitive parameters is given, which lays a theoretical foundation for the accurate establishment of the analytical model.
2) Based on the EMC, Faraday's law, Ampere's law and LPTN, the analytical model of the PMEC including fully sensitive parameters and electromagnetic thermal nonlinearity is established. Combined with the FEM of electromagnetic-thermal multi-field coupling, the comparative study is carried out. The analytical model can accurately analyze the electromagnetic characteristics, temperature characteristics and transmission characteristics of the PMEC with different slip and structural parameters, and the error between the analytical data and the FEM data is less than 4.2%, which verifies the validity of the analytical model.
3) The influence of thermal effect, skin effect and inductive reactance of material electromagnetic parameters on the accuracy of transmission analytical model is studied, and the phenomenon that the error of the unimproved analytical model increases with the increase of slip is repeated. The improved analytical model can accurately analyze the transmission characteristics of the PMEC under different parameters, and it provides reference for the accurate analytical modeling of the PMEC.
4) The experimental study on the electromagnetic characteristics, temperature characteristics and transmission characteristics of the PMEC are carried out, and the improved analytical model, the unimproved analytical model, the FEM and the experiment are compared. The accuracy of the improved analytical model is further proved.

APPENDIX

$$Q_{4-5} = \frac{\lambda_c \pi \left(r_4^2 - r_3^2\right)}{h_c} (t_4 - t_5) \tag{72}$$

$$Q_{4-7} = 2\pi r_4 h_c h_{4-7} (t_4 - t_7) \tag{73}$$

$$Q_{3-4} = h_{3-4}\pi \left(r_4^2 - r_3^2\right) (t_4 - t_3) \tag{74}$$

$$Q_{5-7-1} = h_{5-7-1} A_{5-7} (t_5 - t_7) \tag{75}$$

$$Q_{5-7-2} = \varepsilon_{5-7} \delta_t A_{5-7} \left(t_5^4 - t_7^4\right) \tag{76}$$

$$Q_{3-6} = h_{3-6} A_{3-6} (t_3 - t_6) \tag{77}$$

$$Q_{2-3} = h_{2-3}\pi\alpha \left(r_2^2 - r_1^2\right) (t_3 - t_2) \tag{78}$$

$$Q_{2-6} = \frac{\lambda_r A_{2-6}}{h_r'} (t_2 - t_6) \tag{79}$$

$$Q_{1-7-1} = h_{1-7-1}\pi \left[(r_2 + 0.01)^2 - (r_1 - 0.01)^2\right] (t_1 - t_7) \tag{80}$$

$$Q_{1-7-2} = \varepsilon_{1-7} \delta_t \pi \left[(r_2 + 0.01)^2 - (r_1 - 0.01)^2\right] \left(t_1^4 - t_7^4\right) \tag{81}$$

Q_{4-5} is the heat transferred from copper rotor to copper rotor back iron, Q_{4-7} is the heat transferred from copper rotor to air, Q_{3-4} is the heat transferred from copper rotor to air gap, Q_{5-7-1} is the heat convection of copper rotor back iron, Q_{5-7-2} is the heat radiation of copper rotor back iron, Q_{3-6} is the heat transferred from the air gap to the installed rotor, Q_{2-3} is the heat transferred from air gap to the PMEC, Q_{2-6} is the heat exchanged between the permanent magnet and the installed rotor, Q_{1-7-1} is the heat convection of the PM back iron, Q_{1-7-2} is the heat radiation of the PM back iron.

REFERENCES

[1] L. Ye, D. Li, Y. Ma, and B. Jiao, "Design and performance of a water-cooled permanent magnet retarder for heavy vehicles," *IEEE Trans. Energy Convers.*, vol. 26, no. 3, pp. 953–958, Sep. 2011.
[2] B. Li, H. Ma, X. Yu, J. Zeng, X. Guo, and B. Wen, "Nonlinear vibration and dynamic stability analysis of rotor-blade system with nonlinear supports," *Arch. Appl. Mech.*, vol. 89, no. 7, pp. 1375–1402, Jul. 2019.
[3] A. Wallace, A. von Jouanne, R. Jeffryes, E. Matheson, and X. Zhou, "Comparison testing of an adjustable-speed permanent-magnet eddy-current coupling," in *Proc. Conf. Rec. Annu. Pulp Paper Ind. Tech. Conf.*, Atlanta, GA, USA, 2000, pp. 73–78.
[4] L. Mo, X. Zhu, T. Zhang, L. Quan, Y. Wang, and J. Huang, "Temperature rise calculation of a flux-switching permanent-magnet double-rotor machine using electromagnetic-thermal coupling analysis," *IEEE Trans. Magn.*, vol. 54, no. 3, Mar. 2018, Art. no. 8201004.

[5] J. Fontchastagner, T. Lubin, and D. Netter, "Axial-field eddy-current coupling: A 3D test problem for numerical experiments," *Int. J. Numer. Model., Electron. Netw., Devices Fields*, vol. 31, no. 2, Nov. 2016, Art. no. e2217.
[6] Z. Li, D. Wang, D. Zheng, and L. Yu, "Analytical modeling and analysis of magnetic field and torque for novel axial flux eddy current couplers with PM excitation," *AIP Adv.*, vol. 7, no. 10, Oct. 2017, Art. no. 105303.
[7] M. Ziolkowski and H. Brauer, "Fast computation technique of forces acting on moving permanent magnet," *IEEE Trans. Magn.*, vol. 46, no. 8, pp. 2927–2930, Aug. 2010.
[8] H.-J. Shin, J.-Y. Choi, S.-M. Jang, and K.-Y. Lim, "Design and analysis of axial permanent magnet couplings based on 3D FEM," *IEEE Trans. Magn.*, vol. 49, no. 7, pp. 3985–3988, Jul. 2013.
[9] C. Tian, Y. Zhong, L. Wei, Y. Lei, B. Chen, Y. Gao, K. Muramatsu, and J. Yuan, "A coupled method for evaluating eddy current loss of NdFeB permanent magnets in a saturated core fault current limiter," *IEEE Trans. Magn.*, vol. 53, no. 6, Jun. 2017, Art. no. 6300504.
[10] Y. Kano, T. Kosaka, and N. Matsui, "Simple nonlinear magnetic analysis for permanent-magnet motors," *IEEE Trans. Ind. Appl.*, vol. 41, no. 5, pp. 1205–1214, Sep./Oct. 2005.
[11] A. Canova and F. Freschi, "Multiobjective design optimization and Pareto front analysis of a radial eddy current coupler," *Int. J. Appl. Electromagn. Mech.*, vol. 32, no. 4, pp. 219–236, Apr. 2010.
[12] A. Canova and B. Vusini, "Analytical modeling of rotating eddy-current couplers," *IEEE Trans. Magn.*, vol. 41, no. 1, pp. 24–35, Jan. 2005.
[13] A. Canova, F. Freschi, G. Gruosso, and B. Vusini, "Genetic optimisation of radial eddy current couplings," *COMPEL-Int. J. Comput. Math. Electr. Electron. Eng.*, vol. 24, no. 3, pp. 767–783, Sep. 2005.
[14] J. Wang, H. Lin, S. Fang, and Y. Huang, "A general analytical model of permanent magnet eddy current couplings," *IEEE Trans. Magn.*, vol. 50, no. 1, Jan. 2014, Art. no. 8000109.
[15] Z. Li, D. Wang, and D. Zheng, "Accurate prediction and analysis of electromagnetic fields and forces in flux-focusing eddy current coupling with double slotted conductor rotors," *IEEE Access*, vol. 6, pp. 37685–37699, 2018.
[16] D. Zheng, D. Wang, S. Li, H. Zhang, L. Yu, and Z. Li, "Electromagnetic-thermal model for improved axial-flux eddy current couplings with combine rectangle-shaped magnets," *IEEE Access*, vol. 6, pp. 26383–26390, 2018.
[17] D. Zarko, D. Ban, and T. A. Lipo, "Analytical solution for electromagnetic torque in surface permanent-magnet motors using conformal mapping," *IEEE Trans. Magn.*, vol. 45, no. 7, pp. 2943–2954, Jul. 2009.
[18] X. Dai, Q. Liang, J. Cao, Y. Long, J. Mo, and S. Wang, "Analytical modeling of axial-flux permanent magnet eddy current couplings with a slotted conductor topology," *IEEE Trans. Magn.*, vol. 52, no. 2, Feb. 2016, Art. no. 8000315.
[19] Y. Li, H. Lin, H. Huang, H. Yang, Q. Tao, and S. Fang, "Analytical analysis of a novel brushless hybrid excited adjustable speed eddy current coupling," *Energies*, vol. 12, no. 2, p. 308, Jan. 2019.
[20] B. Kou, Y. Jin, H. Zhang, L. Zhang, and H. Zhang, "Analysis and design of hybrid excitation linear eddy current brake," *IEEE Trans. Energy Convers.*, vol. 29, no. 2, pp. 496–506, Jun. 2014.
[21] S. Mohammadi and M. Mirsalim, "Double-sided permanent-magnet radial-flux eddy-current couplers: Three-dimensional analytical modelling, static and transient study, and sensitivity analysis," *IET Electr. Power Appl.*, vol. 7, no. 9, pp. 665–679, Nov. 2013.
[22] S. Mohammadi, M. Mirsalim, and S. Vaez-Zadeh, "Nonlinear modeling of eddy-current couplers," *IEEE Trans. Energy Convers.*, vol. 29, no. 1, pp. 224–231, Mar. 2014.
[23] V. Aberoomand, M. Mirsalim, and R. Fesharakifard, "Design optimization of double-sided permanent-magnet axial eddy-current couplers for use in dynamic applications," *IEEE Trans. Energy Convers.*, vol. 34, no. 2, pp. 909–920, Jun. 2019.
[24] J. Wang and J. Zhu, "A simple method for performance prediction of permanent magnet eddy current couplings using a new magnetic equivalent circuit model," *IEEE Trans. Ind. Electron.*, vol. 65, no. 3, pp. 2487–2495, Mar. 2018.
[25] J. Wang, H. Lin, and S. Fang, "Analytical prediction of torque characteristics of eddy current couplings having a quasi-Halbach magnet structure," *IEEE Trans. Magn.*, vol. 52, no. 6, pp. 1–9, Jun. 2016. 8001209
[26] X. Yang and Y. Liu, "An improved performance prediction model of permanent magnet eddy current couplings based on eddy current inductance characteristics," *AIP Advances*, vol. 9, Mar. 2019, Art. no. 035350.
[27] X. Yang, Y. Liu, and L. Wang, "Nonlinear modeling of transmission performance for permanent magnet eddy current coupler," *Math. Problems Eng.*, vol. 2019, pp. 1–14, May 2019.
[28] Z. Song, "Rotating core loss model for motor considering skin effect and dynamic hysteresis effect," *Trans. Chin. Soc. Agricult. Eng.*, vol. 35, no. 6, pp. 74–80, Mar. 2019.
[29] H. Greenhouse, "Design of planar rectangular microelectronic inductors," *IEEE Trans. Parts, Hybrids, Packag.*, vol. PHP-10, no. 2, pp. 101–109, Jun. 1974.
[30] S. Jenei, B. K. J. C. Nauwelaers, and S. Decoutere, "Physics-based closed-form inductance expression for compact modeling of integrated spiral inductors," *IEEE J. Solid-State Circuits*, vol. 37, no. 1, pp. 77–80, Jan. 2002.
[31] R. L. Russell and K. H. Norsworthy, "Eddy currents and wall losses in screened-rotor induction motors," *Proc. IEE A, Power Eng.*, vol. 105, no. 20, pp. 163–175, Apr. 1958.
[32] X. Huang, L. Li, B. Zhou, C. Zhang, and Z. Zhang, "Temperature calculation for tubular linear motor by the combination of thermal circuit and temperature field method considering the linear motion of air gap," *IEEE Trans. Ind. Electron.*, vol. 61, no. 8, pp. 3923–3931, Aug. 2014.
[33] Q. Lu, X. Zhang, Y. Chen, X. Huang, Y. Ye, and Z. Q. Zhu, "Modeling and investigation of thermal characteristics of a water-cooled permanent-magnet linear motor," *IEEE Trans. Ind. Appl.*, vol. 51, no. 3, pp. 2086–2096, May 2015.
[34] Y. Jin, L. Li, B. Kou, and D. Pan, "Thermal analysis of a hybrid excitation linear eddy current brake," *IEEE Trans. Ind. Electron.*, vol. 66, no. 4, pp. 2987–2997, Apr. 2019.
[35] L. Mao and H. Ye, "Thermal analysis of thermophotovoltaic system applying the radation resistor network method," *ACTA Energiae Solaris Sinica*, vol. 31, no. 1, pp. 54–59, Jan. 2010.

XIAOWEI YANG received the bachelor's degree in mechanical electronics from Shandong Jianzhu University, and the master's degree in control engineering from Beihang University. He is currently pursuing the Ph.D. degree in mechanical electronics with Beihang University. His research interests include nonlinear active vibration control, smart material and structure, giant magnetostrictive actuator, and magnetic coupling transmission technology.

YONGGUANG LIU was born in Heilongjiang, China, in 1967. He received the Ph.D. degree in mechanical engineering from the Harbin University of Technology, Harbin, China, in 1994 and 1999, respectively.

He was a Postdoctoral Research with Tsinghua University, from 1999 to 2001. Since 2002, he has been working as an Associate Professor with the Department of Mechatronic, Beihang University. His research interests include hydraulic servo control, industrial robots, network control, giant magnetostrictive actuator, nonlinear active vibration control, and magnetic coupling transmission technology.

LIANG WANG was born in 1962. He graduated from the Harbin institute of Marine engineering, in 1985. He received the M.S. degree in fluid transmission and control specialty from the Harbin Institute of Technology, in 1988, and the Ph.D. degree from Beihang University, in 2000.

He was a Postdoctoral Research with the Beihang University, from 2000 to 2002. Since 2002, he has been taught with the Department of Mechanical and Electronic Engineering, Beihang Automation College. He is a Professor of mechanical and electronic engineering and the Ph.D. supervisor. In 2005, he also serves as the Director of the Engineering Training Center (National demonstration Center), Beihang University. His research interests include hydraulic servo control, electro-hydraulic servo drive mechanism and control, robot mechanism and control technology, electromagnetic drive, and control.